Predictability of Non-Phase-Locked Baroclinic Tides in the Caribbean Sea

Edward D. Zaron[1]

[1]Department of Civil and Environmental Engineering, Portland State University, Portland, Oregon, USA

Correspondence: E. D. Zaron (ezaron@pdx.edu)

Abstract. The predictability of the sea surface height expression of baroclinic tides is examined with 96 hr forecasts produced by the AMSEAS operational forecast model during 2013–2014. The phase-locked tide, both barotropic and baroclinic, is identified by harmonic analysis of the 2 year record and found to agree well with observations from tide gauges and satellite altimetry within the Caribbean Sea. The non-phase-locked baroclinic tide, which is created by the time-variable mesoscale

5   stratification and currents, may be identified from residual sea level anomaly (SLA) near the tidal frequencies. The predictability of the non-phase-locked tide is assessed by measuring the difference between a forecast – centered at T+36 hr, T+60 hr, or T+84 hr – and the model's later verifying analysis for the same time. Within the Caribbean Sea, where a baroclinic tidal sea level range of ± 5 cm is typical, the forecast error for the non-phase-locked tidal SLA is correlated with the forecast error for the sub-tidal (mesoscale) SLA. Root-mean-square values of the former range from 0.5 cm to 2 cm, while the latter ranges from

10   1 cm to 6 cm, for a typical 84 hr forecast. The spatial and temporal variability of the forecast error is related to the dynamical origins of the non-phase-locked tide and is briefly surveyed within the model.

1   Introduction

Sea level fluctuations of several centimeters associated with the astronomically-forced baroclinic tide are nearly ubiquitous throughout the ocean (Ray and Mitchum, 1996; Zhao et al., 2016). While they are a relatively small component of the sea level

15   variability spectrum, they can be the dominant source of variability for wavelengths between, roughly, 100 km and 180 km, particularly near their sources (Ray and Zaron, 2011; Zaron, 2017). This component of sea level variability is also associated with subsurface isopycnal variability and baroclinic currents. Baroclinic tides are sometimes regarded as a source of high-frequency noise in ocean observations; however, they are of interest in their own right because of the momentum, energy, and material transports associated with these waves.

20   It is of interest to know the degree to which baroclinic tidal sea level variability can be predicted. The long record of observations from satellite altimeters has enabled the identification and mapping of the baroclinic sea level phase-locked with the astronomical tidal forcing. This component of sea level is predictable from the orbital elements of the sun and moon, and it is found to closely obey the theoretically-predicted dispersion relation for linear waves propagating through the ocean's time-mean stratification (Dushaw, 2002; Zhao et al., 2011; Ray and Zaron, 2016). However, there is another component of sea

25   level variability associated with the tidal frequencies that represents non-phase-locked baroclinic tides, which are created by

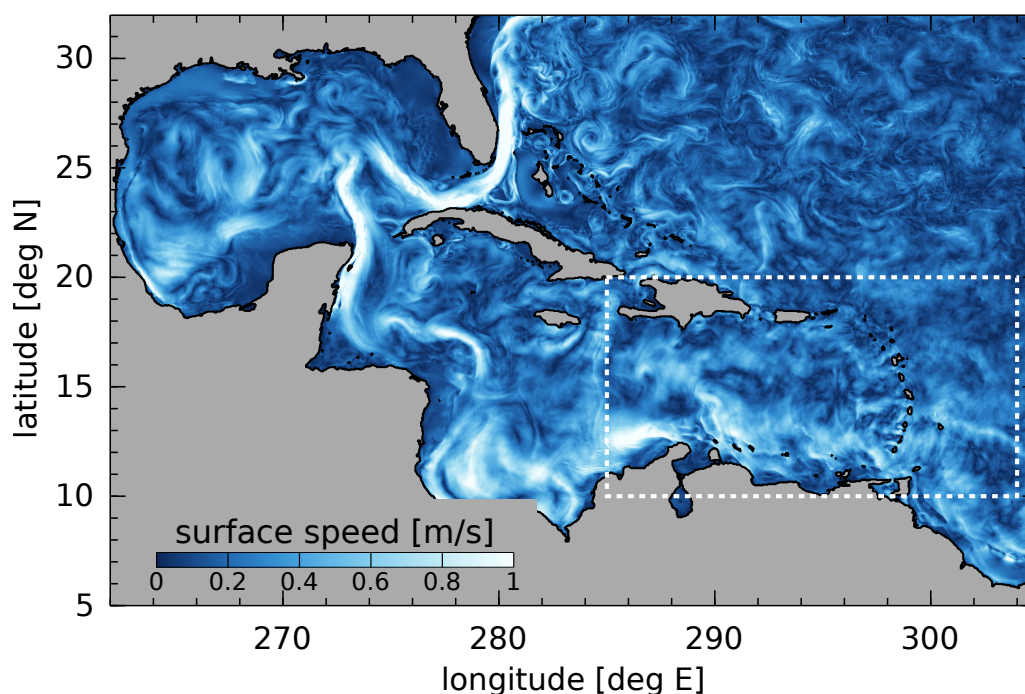Ocean Science
Discussions

Open Access

EGU

Figure 1. AMSEAS model domain. This snapshot of surface currents from the arbitrary representative date, 2013-02-01, shows prominent features of ocean circulation in the Western Atlantic, namely the Loop Current in the Gulf of Mexico and the Florida Current. The rectangular box (dashed white line) indicates the region shown in subsequent plots.

temporal modulations of the propagation medium (Munk and Cartwright, 1966; Rainville and Pinkel, 2006; Colosi and Munk, 2006; Zilberman et al., 2011; Ray and Zaron, 2011). Because modulations of the propagation medium – caused by mesoscale eddies and other processes – are, in part, represented within operational ocean forecasting systems, it ought to be possible to predict some component of the non-phase-locked tide with such a forecasting system.

5   This paper investigates the predictability of sea level associated with the non-phase-locked baroclinic tide in the AMSEAS model, a state-of-the-art operational ocean forecasting system. Preparation for the Surface Water & Ocean Topography (SWOT) swath altimeter mission, planned for launch in 2021, is concerned with distinguishing balanced motion from inertia-gravity waves in sea surface topography data (Gaultier et al., 2016; Zaron and Rocha, 2018), and the sea surface expression of baroclinic tides is a prominent manifestation of inertia-gravity waves. The present study provides a baseline measure of model

10   forecast skill which will be useful for evaluating future improvements in forecasting baroclinic tides. The results quantify the forecast skill and provide insight into the phenomenology of internal tide signals as represented in high-resolution ocean models.
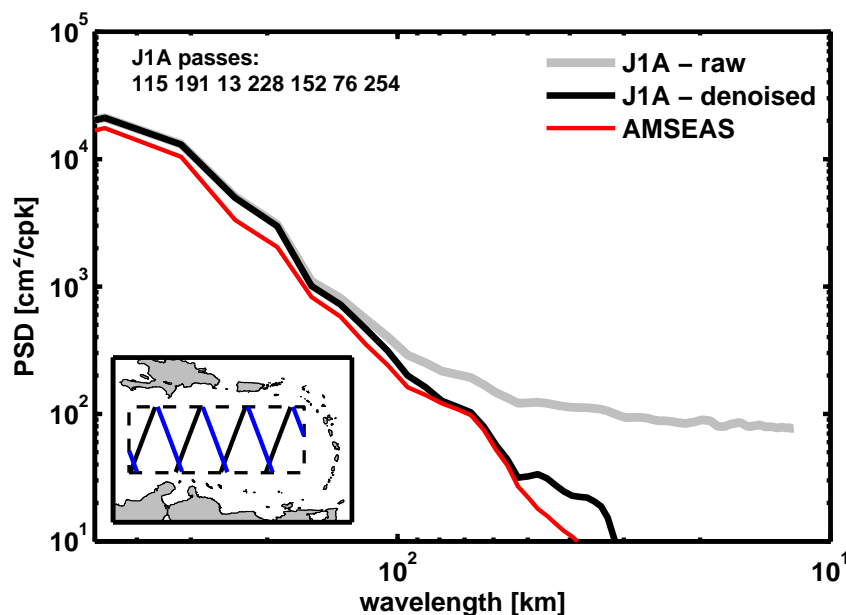
Figure 2. Along-track sea-surface height wavenumber spectra, AMSEAS vs. Jason-1. The spectra are periodograms averaged over the Jason-1 tracks within the Caribbean (inset), for the period 2010–2012 for AMSEAS and 2002–2009 for Jason-1. The denoised Jason-1 spectrum (black) is obtained by subtracting a white noise spectrum estimated from scales smaller than 30 km in the raw Jason-1 spectrum (gray). The denoised Jason-1 spectrum compares well with the AMSEAS spectrum (red).

2   The AMSEAS ocean forecasting system

The AMSEAS model is a 1/30-degree (approx. 3.5 km), 40-level, implementation of the Navy Coastal Ocean Model (NCOM; Kara et al., 2006) which has been producing operational forecasts of the Caribbean Sea, Gulf of Mexico, and Western Atlantic since May 2010. The model is re-initialized daily by assimilating observations using the Navy Coupled Ocean Data Assimi-

5 lation System (NCODA; Cummings, 2011) and integrated to produce a 96-hour forecast by the Naval Oceanographic Office (NAVOCEANO). Prior to April 2013, AMSEAS was forced by wind stress and heat flux from the Fleet Numerical Meteorology and Oceanography Center's Navy Operational Global Atmospheric Prediction System (NOGAPS; Rosmond et al., 2002), and lateral open boundary conditions for temperature, salinity, and non-tidal surface elevation were provided by operational Global NCOM (Barron et al., 2007). Since April 2013, the atmospheric forcing has been provided by the Navy Global Environmental

10 Model (NAVGEM; Hogan et al., 2014), with lateral boundary conditions provided by operational Global HYCOM (Metzger et al., 2014). Tides are not provided by the global model presently used for boundary conditions; instead, tides predicted with the OTIS barotropic tide model (Egbert and Erofeeva, 2002) are added to the barotropic currents and sea surface height data at open boundaries. In addition, the tide-generating force is applied within the model domain, and incorporates the effects of ocean loading and self-attraction consistent with the OTIS model.
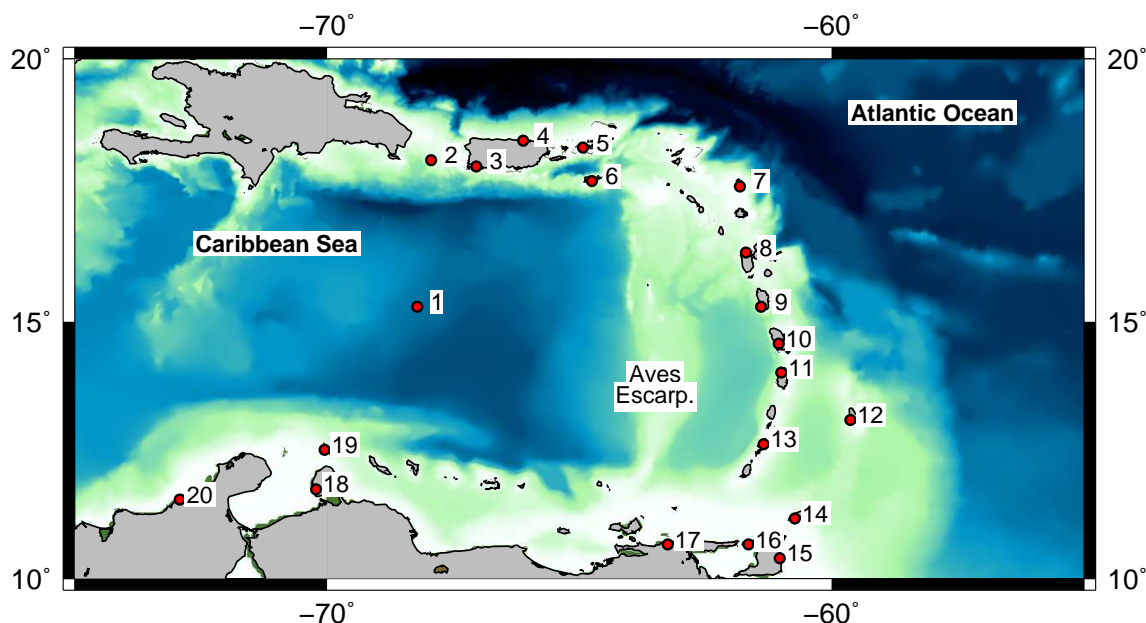
Ocean Science

Discussions

Open Access

EGU

Figure 3. Caribbean Sea and tide gauge locations. Tide gauge stations are numbered clockwise around the Caribbean Sea, starting at station 1, DART-42407 (see Table A1). Some closely-spaced stations are not plotted. Significant sites of internal tide generation are Mona Passage (near station 2), Anagada Passage (east of stations 5 and 6), and the passages between the southern Windward Islands (stations 9 to 13) and Grenada Passage (between stations 13 and 17).

The spatial domain of AMSEAS covers the Gulf of Mexico, Caribbean Sea, and a portion of the northeast Atlantic Ocean (Figure 1). The major current systems such as the Yucatan Current, Loop Current, and Florida Current are well-represented in the model, as well as a broad spectrum of variability related to mesoscale eddies, wind-driven circulation, and tides, consistent with historical observations (Carton and Chao, 1999; Centurioni and Niiler, 2003; Torres and Tsimplis, 2012).

5   AMSEAS nowcast/forecast products have been used and validated in a number of studies. For example, Lagrangian trajectories and forecasts were used to interpret biological observations in the Gulf of Mexico (Nero et al., 2013; O'Conner et al., 2016), and skill assessment efforts in the Gulf of Mexico have been reported (Hernandez et al., 2015; Zaron et al., 2015). AMSEAS was used to provide boundary conditions for a high-resolution regional forecasting system around Puerto Rico and the U.S. Virgin Islands, and validated through comparisons with tide gauge and water current measurements (Solano et al., 10   2018). Figure 2 shows a comparison of sea surface height wavenumber spectra from AMSEAS versus Jason-1 satellite altimetry within the eastern and central Caribbean Sea. The overall slope and energy level of the one-dimensional spectra are in good agreement. The small offset between the observed and modeled spectra may be explained by the different time periods used for computing the spectra, which is the 2010–2012 period for AMSEAS and the 2002–2009 period for Jason-1.

     For later reference it is useful to refer to Figure 3 which shows the bottom topography in the region of study, from 0 m to 15   6000 m depth. A major topographic feature of the Eastern Caribbean, Aves Escarpment, is indicated, as are the locations of 17 tide gauge sites, including one bottom pressure gauge (site 1). Evidence for the range of dynamics active in AMSEAS is
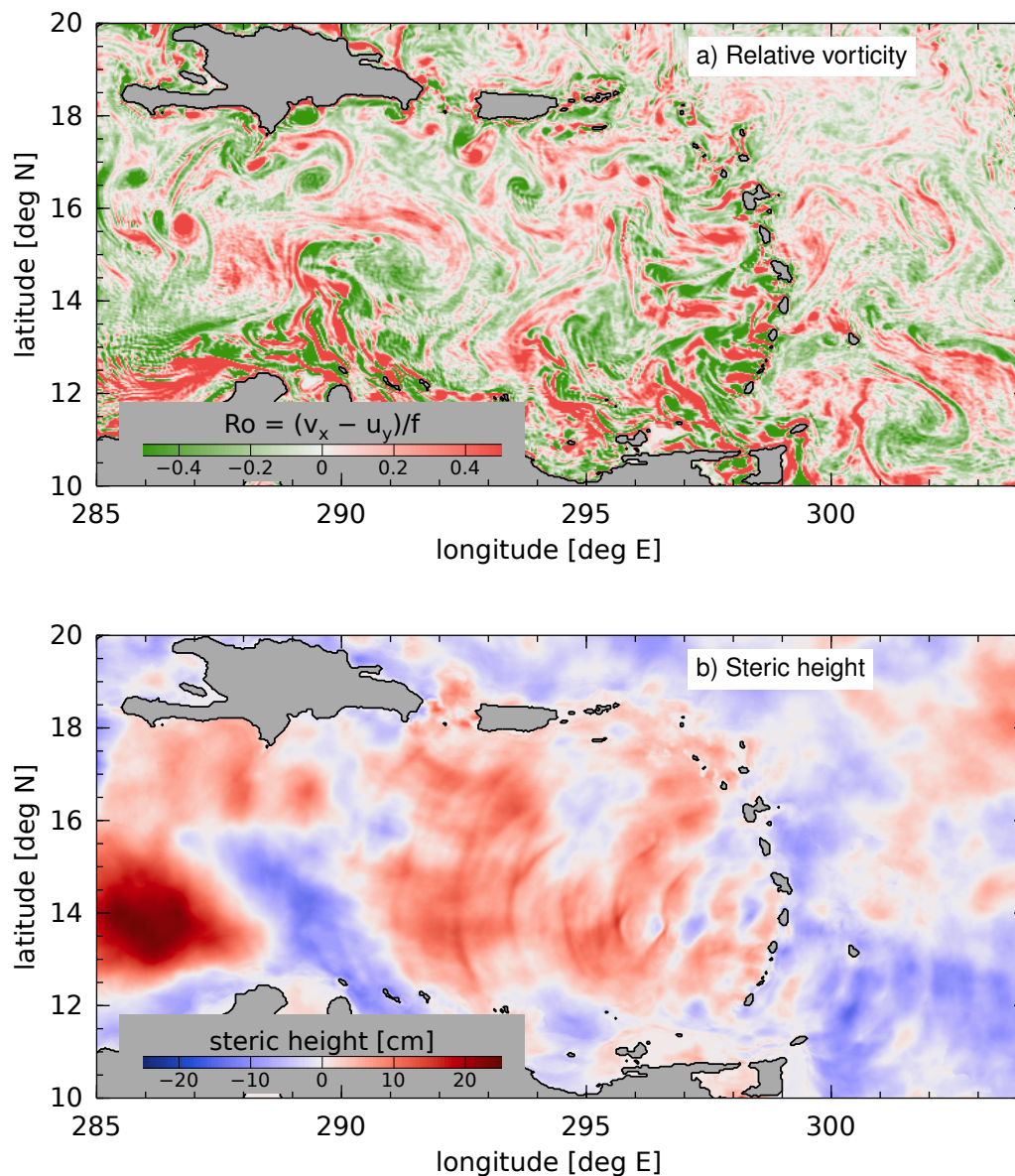
Ocean Science
Discussions
Open Access
EGU

Figure 4. Snapshots of AMSEAS model outputs valid on 2013-02-01. (a) Relative vorticity field (expressed as a Rossby number) contains a spectrum of small circular eddies and filamentous structures. (b) Steric height anomaly (relative to the 2-yr. average).

shown by the sanpshots of the vertical component of relative vorticity at the ocean surface and the steric height in Figure 4. The relative vorticity field exhibits the attributes of eddies and filaments associated with meso- and sub-mesoscale turbulence in the model. The snapshot of steric height exhibits both large-scale features associated with mesoscale eddies, as well as radially-coherent features associated with propagating internal gravity waves, specifically, the baroclinic tide.
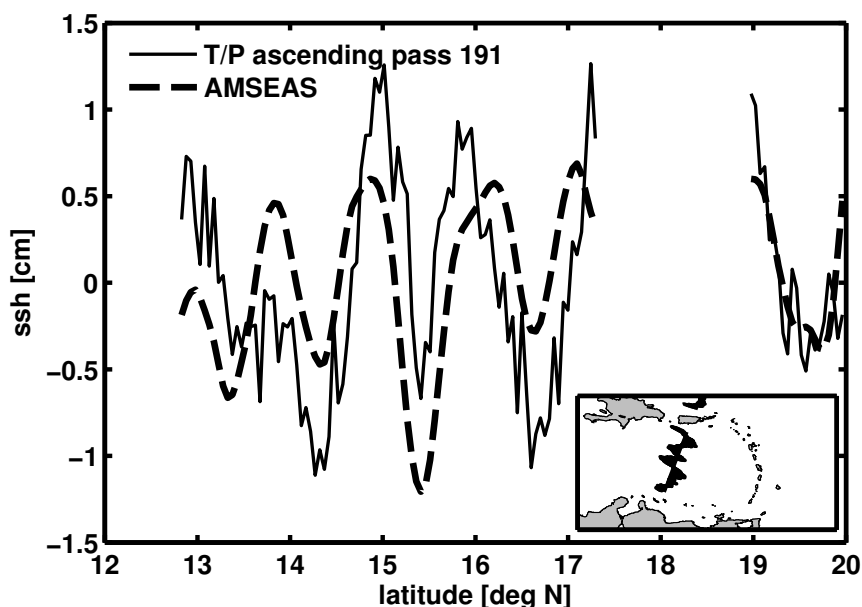
Figure 5. Internal tide along Jason-1 track #191. The in-phase component of the high-passed M_2 tide has maximum peak-to-peak amplitude of 1.5cm in AMSEAS (dashed), and slightly larger amplitude in the altimeter data (solid). Alignment of peaks and troughs is good, particularly near the apparent generation site, Mona Passage, west of Puerto Rico (inset).

3 Phase-locked tides in AMSEAS

The present effort analyzes AMSEAS output from the two-year period, January 2013 – December 2014. For a given date T, AMSEAS produces a nowcast valid at $T + 0$ hr, and forecasts every 3 hours, up to $T + 96$ hr, except for occasional interruptions. The output fields of temperature and salinity, available at 40 vertical levels, have been processed to derive the steric height anomaly at the ocean surface relative to the ocean bottom (IOC et al., 2010). The AMSEAS output sea level anomaly (SLA),

5   which is the sum of both the barotropic and baroclinic (steric) signals, and the derived steric height, have been subjected to least-squares harmonic analysis to identify the phase-locked tides at the M_2, S_2, K_2, N_2, $2N_2$, K_1, O_1, P_1, and Q_1 frequencies (provided through tidal open boundary conditions) and at the M_3, MS_4, M_4, and MN_4 over-tide frequencies (generated by the model's nonlinear dynamics). Note that S_4 and higher frequencies may be present in the model, but they are aliased by the

10 3-hour time sampling. Also, note that any given date-time may contain up to five different estimates for the SLA and steric height from the nowcast ($T + 0$ hr) and the forecasts (from $T + 3$ hr to $T + 96$ hr in three hour increments); the harmonic analysis is computed as an unweighted least-squares fit to all the data, including the overlapping forecasts.

A detailed comparison between the modeled and observed phase-locked M_2 and K_1 tides at the sites indicated in Figure 3 is provided in Appendix A. The main features of the observed tide are reproduced in the model. These include a counter-

15 clockwise propagation of the M_2 tide around an amphidrome in the northeast Caribbean and standing-wave-like behavior of K_1, exhibiting maximum amplitude of about 10 cm along the southern coast (Kjerfve, 1981; Torres and Tsimplis, 2011).

The curvature of the wave-like features in Figure 4b suggests that the baroclinic tide is generated at a relatively small number of sites, namely, at Mona Passage between the Dominican Republic and Puerto Rico (18°N, 292°E), and along the southern Windward Islands (14°N, 298°E; see caption of Figure 3). Satellite altimeter ground tracks are not dense enough to map the baroclinic tides accurately in the Caribbean; however, the signals are unmistakable along individual tracks. Figure 5 compares the in-phase component of the M_2 tide in AMSEAS with the same quantity inferred from the long record of altimetry along a track which passes south of Mona Passage. The peaks and troughs are roughly aligned in the model and observations, and the amplitude of the waves are quite similar in mid-basin, although the values certainly differ in detail.

Further study would be needed to identify in detail the causes for discrepancies between the modeled and observed baroclinic tides. Several factors are likely to be involved, as follows. With regard to the AMSEAS model, it is likely that the resolution is not sufficient to represent the details of the baroclinic tide generation sites. Although the baroclinic tide SLA field is predominantly a mode-1 phenomena, with wavelength in excess of 100 km, achieving quantitative accuracy depends on resolving the detailed seafloor topography of the generation sites; based on experience at the Hawaiian Ridge, this requires a horizontal resolution of 1–2 km (Zaron and Egbert, 2006; Zaron et al., 2009). Also, while the distinction between barotropic and baroclinic sea level is unambiguous in the model, this same distinction cannot be made with observations, and some of the discrepancy is the result of errors in the barotropic tidal corrections, and noise related to non-tidal signals in the observations. Non-phase-locked tidal variability may also contribute to the differences between the model and observations, but to a degree which is presently unknown.

The above remarks concerning the difficulty with mapping the baroclinic tides motivate the methodology used to assess the forecast error of non-phase-locked tides in AMSEAS. In the nomenclature of numerical weather forecasting, the approach taken is a self-analysis verification, or self-verification (e.g., Privé and Errico, 2015). The forecast error is measured by comparing the nowcast valid at date, T_n, with a forecast previously computed on the date, $T_f = T_n - \tau$, with a given lead-time, τ, i.e., $T_f + \tau = T_n$. This approach may be contrasted with a forecast verification based on independent observations, in which the forecast and observations are compared directly as the latter become available. The self-verification is likely to lead to an optimistic estimate of the forecast error, but in the present case, it appears to be the only feasible approach to assessing the predictability of the non-phase-locked tide. The reason for this has more to do with the available data rather than the forecast system, since there are no data which can reliably distinguish non-phase-locked and phase-locked tidal variability over the time and space scales represented within the AMSEAS forecasts.

4 Non-phase-locked tides

The definition of the phase-locked tide is unambiguous since it is defined by constant phase with respect to the known astronomical tidal potential. Defining the non-phase-locked tide is potentially ambiguous since it involves the distinguishing tide-band and non-tidal variability, which implicitly requires either a dynamical definition or a definition based on frequency bandwidth. In addition, a bandwidth-based definition must be meaningful within the available duration of each forecast, which is only four days (from $T + 0$ to $T + 96$ hr). The approach taken here is to define the non-phase-locked tide with respect to
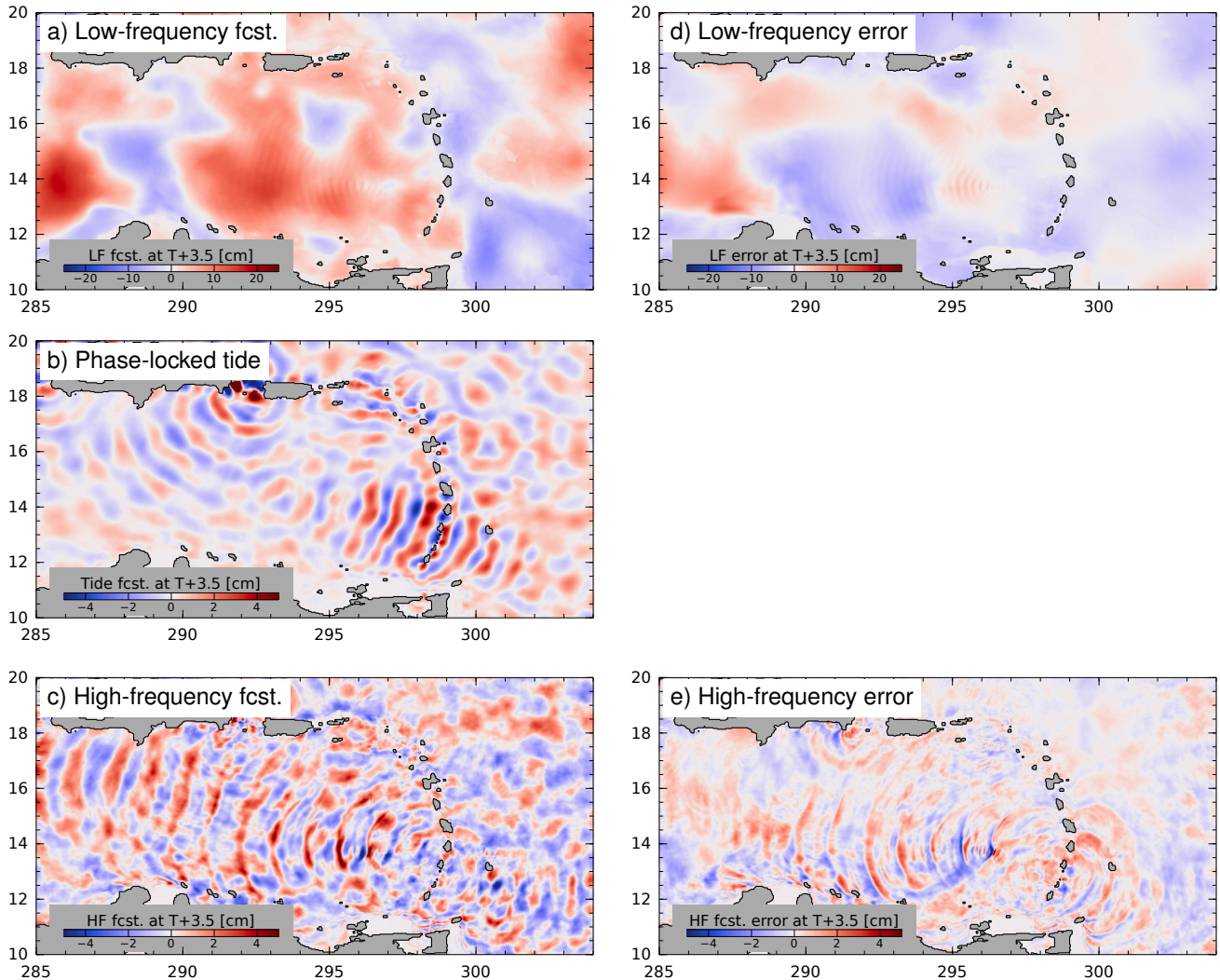
Figure 6. Forecast decomposition and errors. For the purpose of analysis, the steric height forecast is decomposed into a sum of three components: (a) low-frequency (24-hour average), (b) phase-locked tide, and (c) high-frequency (residual). The forecast error is defined as the forecast minus the verifying analysis, valid at the same time. The two components of the forecast error are (d) the low-frequency component, and (e) the high-frequency component; the phase-locked tide is identical in the forecast and the analysis. Note different color scales shown for the high- and low-frequency components.

the daily average of the de-tided steric height. In other words, a tidal prediction is computed using the complex harmonic constants for the 13 astronomically-forced and compound tides described previously, and this predicted tide is removed from the steric height. Then, the daily average of the de-tided steric height is computed centered at noon of each forecast day ($T + 12$, $T + 36$, $T + 60$, and $T + 84$ hr) to provide an estimate of the low-frequency steric height field. The residual field, the de-tided steric height minus its daily average, contains both the non-phase-locked tidal variability plus a small amount of non-tidal high-frequency variability. Note that this analysis approach is applied to steric height rather than the full SLA field; the latter

contains significant high-frequency barotropic variability related to forcing by winds and atmospheric pressure in addition to tides.

This methodology provides a pragmatic definition of the non-phase-locked tidal steric height valid at $T+12, T+36, T+60$, and $T+84$ hr. Alternative approaches could be envisioned, perhaps involving bandpass filtering or complex demodulation,

5   but they would be problematic due to phase errors near the start and end of the 4-day forecast windows. The present approach is relatively simple to implement and explain, and it unambiguously partitions the steric height variance between the low-frequency motion, phase-locked tides, and high-frequency processes, the latter being dominated by non-phase-locked tides. Henceforth the high-frequency component shall simply be referred to as the non-phase-locked tide. The fields centered at $T+12$ hr shall be regarded as the verifying analyses (nowcast) which are to be compared with the forecasts from 3 previous

10   days, at $(T-24)+36$, $(T-48)+60$, and $(T-72)+84$. To shorten the notation, forecasts at these lead times will be denoted with the time offset in days, as "T+1.5", "T+2.5", and "T+3.5", in subsequent figures.

The decomposition of the steric height field just described is illustrated in Figure 6 for the representative date, 2013-02-01. The low-frequency component of the forecast steric height (Fig. 6a) resembles a spatially-smoothed version of the snapshot shown previously (Fig. 4b), except it is obtained by temporal, rather than spatial, averaging. The small-scale waves in Figure 4b

15   are the sum of the predicted tide (Fig. 6b) plus the high-frequency residual (Fig. 6c). The panels in the left column of Figure 6 are valid on $T = $ 2013-02-01T12:00:00, but they were forecast 3.5 days prior, on $T_f = T - 84$ hr $= $ 2013-01-29T00:00:00; the right panel shows the errors in the forecasts, computed by subtracting the nowcast at $T_n = T$. The low-frequency error field (Fig. 6d) is relatively smooth and takes on largest values in the southeast, near the edge of the continental shelf where relatively large currents are present (13°N, 287°E; cf., Fig. 1). The error in the high-frequency component of the steric height (Fig. 6e)

20   exhibits wavelike features. For this particular date, it is clear that the magnitudes of the forecast error fields (right panels) are smaller than the forecasts themselves (left panels); however, the error fields are non-random and display the features one might associate with difficult-to-forecast components of the flow field, e.g., small scales and high-current zones. Note that the range of steric heights shown in panels (a) and (d) is different from that used in the other panels of Figure 6.

To illustrate the character of the forecast errors as a function of increasing lead time, τ, Figure 7 shows the sum of the low-

25   and high-frequency steric height errors for three lead times, $\tau = 1.5, 2.5$, and 3.5 days, valid on the same date as above. The steric height signal associated with mesoscale features is in the range, ± 20 cm, which is much larger than the range, ± 5 cm, associated with the baroclinic tide. The magntiude of the forecast error associated with the low-frequency flow is somewhat larger than the magnitude of the error associated with the high-frequency flow (cf., Fig. 6d and e), but their increase in time is evident in Figure 7. Forecast errors of the low- and high-frequency SLA components exhibit different dynamical features, with

30   wave fronts prominent in the high-frequency component.

5   Results

Given the above decomposition of the nowcast/forecast steric height fields, the statistics of the forecast errors have been computed for the two year period, 2013-2014.
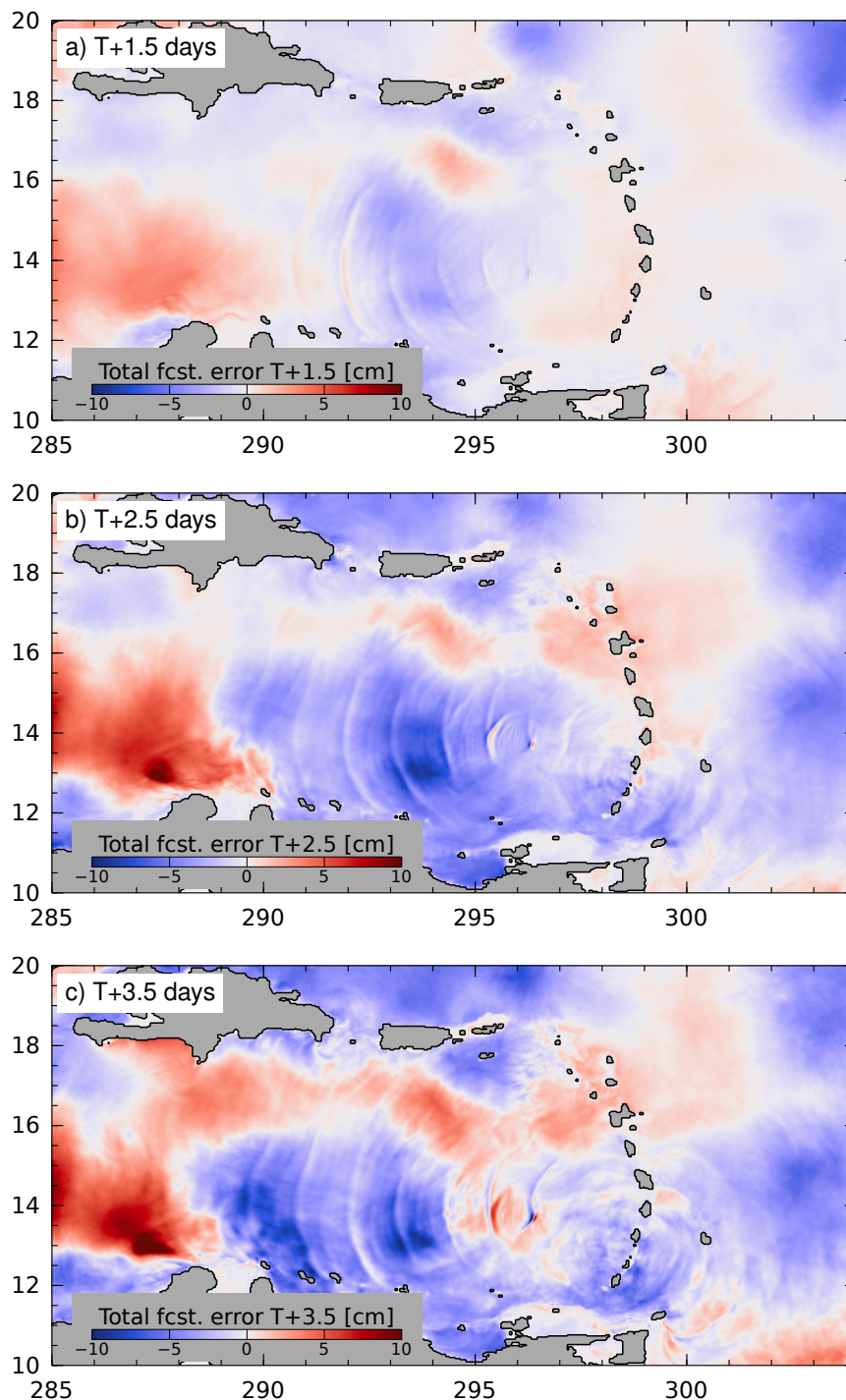
Figure 7. The steric height forecast error for different lead times: (a) T+1.5 days, (b) T+2.5 days, (c) T+3.5 days. Note that the color scale differs from previous figures; it was chosen to make the error growth visible as a function of increasing forecast lead time.
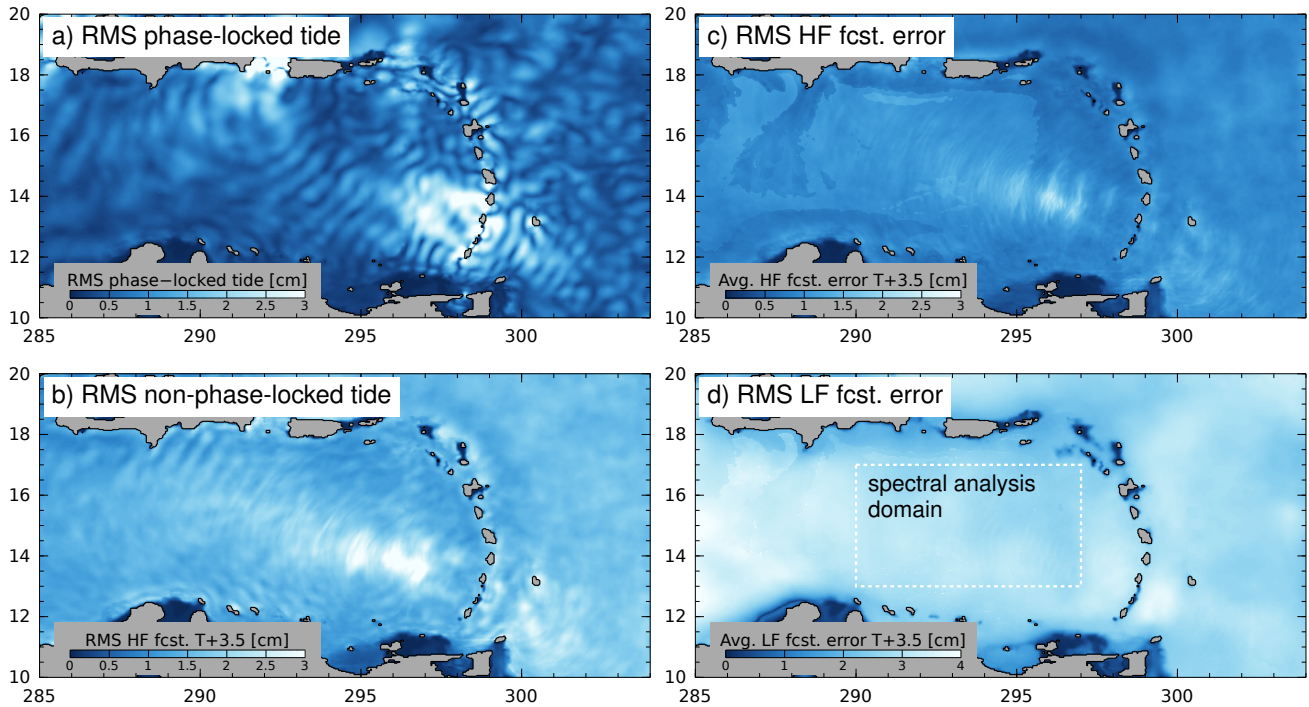
Figure 8. Root-mean-square (RMS) (a) phase-locked tide, (b) non-phase-locked tide, (c) high-frequency forecast error at T+3.5 days, (d) low-frequency forecast error at T+3.5 days. The "spectral analysis domain" in (d) indicates the region used for the computation of the radial wavenumber spectra in Figure 10, below; it is also the region of spatial averaging for the forecast errors summarized in Figure 9.

A summary of the spatial statistics is provided in Figure 8 which shows the root-mean-square steric height attributed to the forecast phase locked tide (a) and the non-phase-locked tide (b), together with the forecast error of the non-phase-locked tide (c) and the low-frequency SLA (d). The first observation to make from these figures is that the spatial distribution of the (forecast) phase-locked and non-phase-locked tides differs. The amplitude of the phase-locked tide is largest near its sources

5 in Mona Passage and the Windward Islands (Fig. 8a), while the non-phase-locked tide is largest around Aves Escarpment, some distance from the wave source along the Windward Islands (Fig. 8b). The peak amplitudes of both fields are of similar magntiude. Note the scale of the root-mean-square amplitude, 3 cm, is much smaller than the root-mean-square amplitude of the low-frequency steric height associated with the mesoscale, about 20 cm (not shown).

The error for the $T + 3.5$ day forecast of the high-frequency steric height component (Fig. 8c) is smaller in magnitude than

10 the root-mean-square value (Fig. 8b), and it is even more confined to the southern part of the Aves Escarpment. In contrast, the forecast error for the low-frequency flow component is spatially uniform (Fig. 8d), except for the effect of water depth on the steric height anomaly.

Because the non-phase locked tide arises as a consequence of the time-variable propagation medium, it was hypothesized that the forecast error for the non-phase-locked tide would be related to the forecast error for the low-frequency flow. This
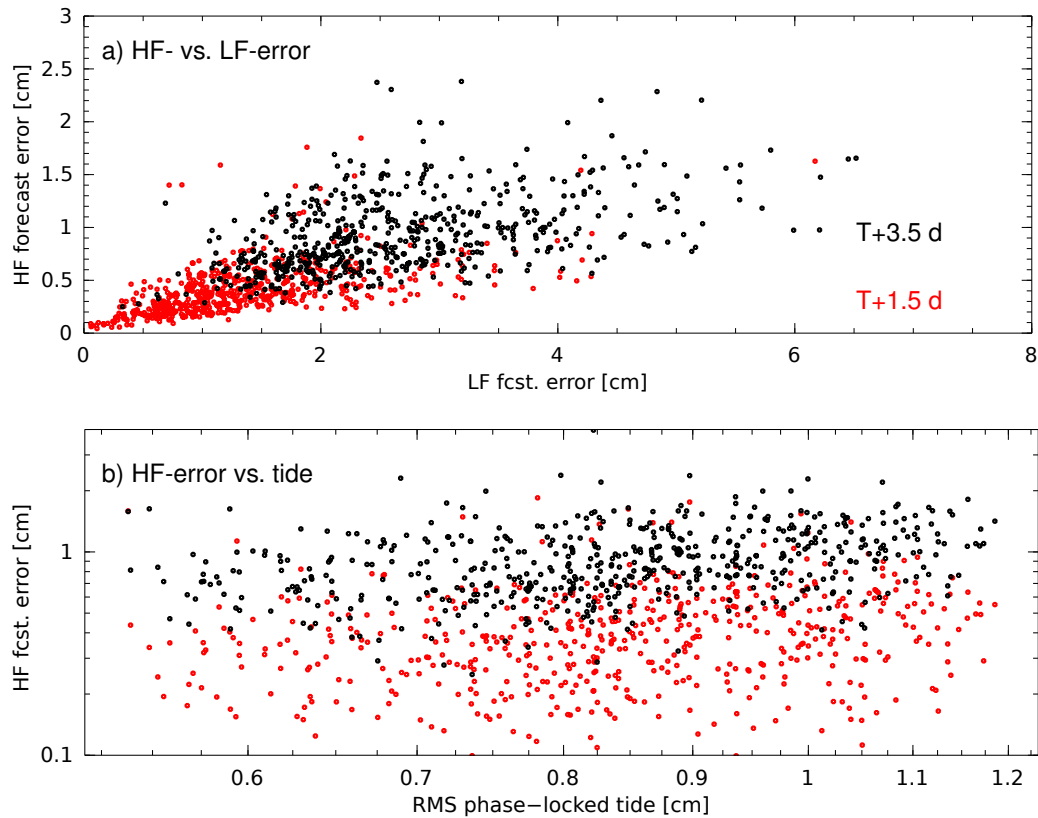
Ocean Science
Discussions

Figure 9. High-frequency (HF) forecast error. (a) HF forecast error is an increasing function of LF forecast error, and error increases as a function of lead time (T+1.5 days shown in red, T+3.5 days shown in black). (b) HF forecast error depends weakly on the phase-locked tide (red and black dots as in (a)).

hypothesis is generally confirmed by the statistics in Figure 9a, which shows the high-frequency error as a function of the low-frequency error. The forecast errors for the two components of the steric height are positively correlated (note that the errors reported here are root-mean-square averages over the domain denoted, "spectral analysis domain" in Figure 8d); however, there is considerable scatter in the high-frequency error which is unrelated to the low-frequency error. A plot of the forecast error

5   versus the amplitude of the phase-locked tide (Fig. 9b) indicates that the error is only weakly dependent on the phase-locked tide (e.g., the spring-neap cycle). The scatter of the high-frequency error with respect to these root-mean-square statistics is consistent with the genesis of the errors at small-scale features which are inherently less predictable and constrained by observations. Note that the errors for the $T+3.5$ day forecasts (black dots) are larger than for the $T+1.5$ day forecasts (red dots), as would be expected (cf., Fig. 7).

10   A spectral analysis of the steric height anomaly has been conducted in order to better understand the spatial structure of the forecast error in relation to the fields themselves. The radial power spectrum, shown in Figure 10, is computed by azimuthally
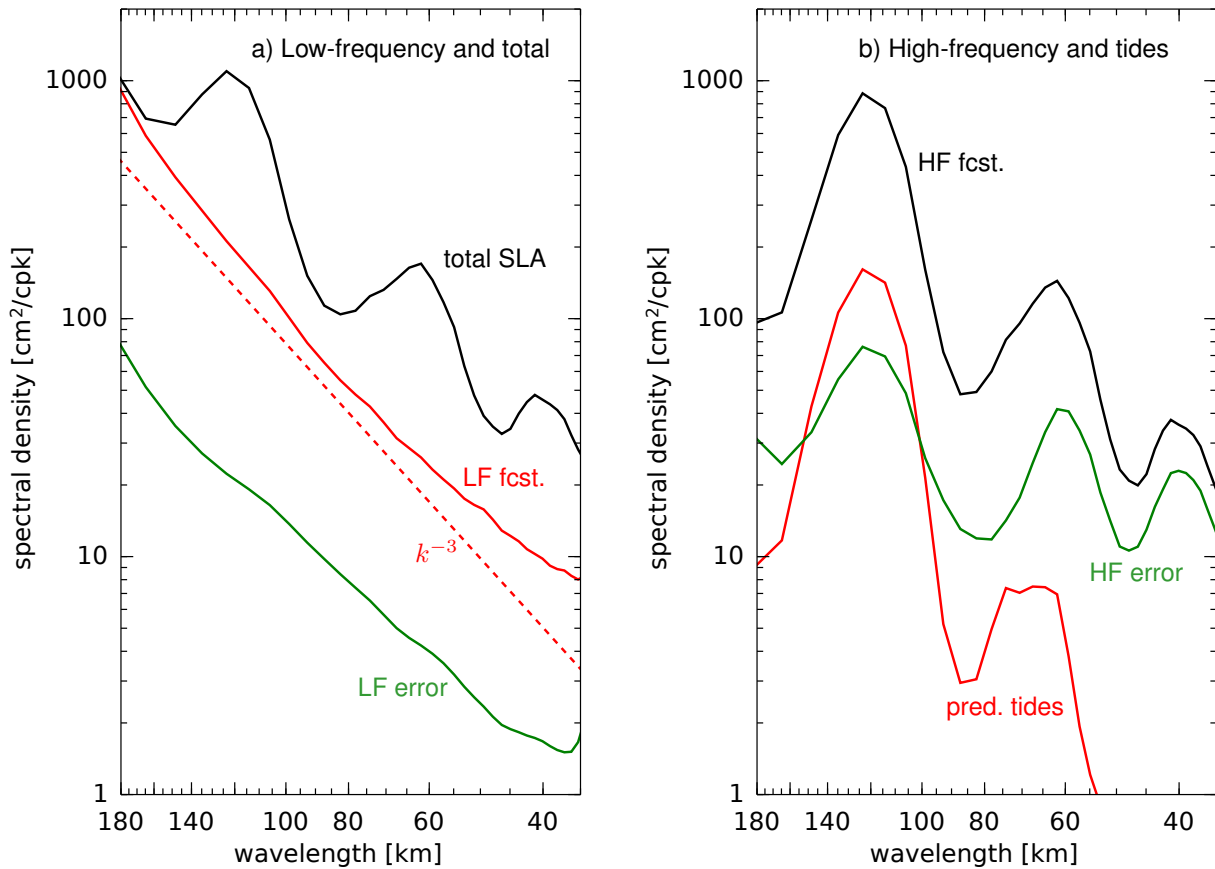
Figure 10. Wavenumber power spectra for (a) low-frequency, and (b) high-frequency SLA components. The k^{-3} wavenumber dependence in panel (a) is shown for reference.

averaging the 2-dimensional power spectrum (within the "spectral analysis domain" indicated in Fig. 8d), and clearly exhibits peaks related to the baroclinic tide (compare the curve labelled *total SLA* in Fig. 10a with the 1-dimensional AMSEAS spectrum in Fig. 2). The tidal peaks are completely absent in the low-frequency forecast and its error (red and green lines, respectively, in Fig. 10a). In contrast, the tidal peaks dominate the spectra of the high-frequency steric height (Fig. 10b). The variance associated with the mode-1 semidiurnal baroclinic tide, at a wavelength of 120 km, is partly associated with the predictable phase-locked tide (red line), and the forecast error (green line) is less than 10% of the total high-frequency forecast variance (black line). At wavelengths shorter than the mode-1 wave, the high-frequency forecast error is both larger than the phase-locked tide and it is occupies an increasing fraction of the total high-frequency variance. In other words, as would be expected, the baroclinic tides are increasingly less phase-locked, and less predictable, at smaller scales.
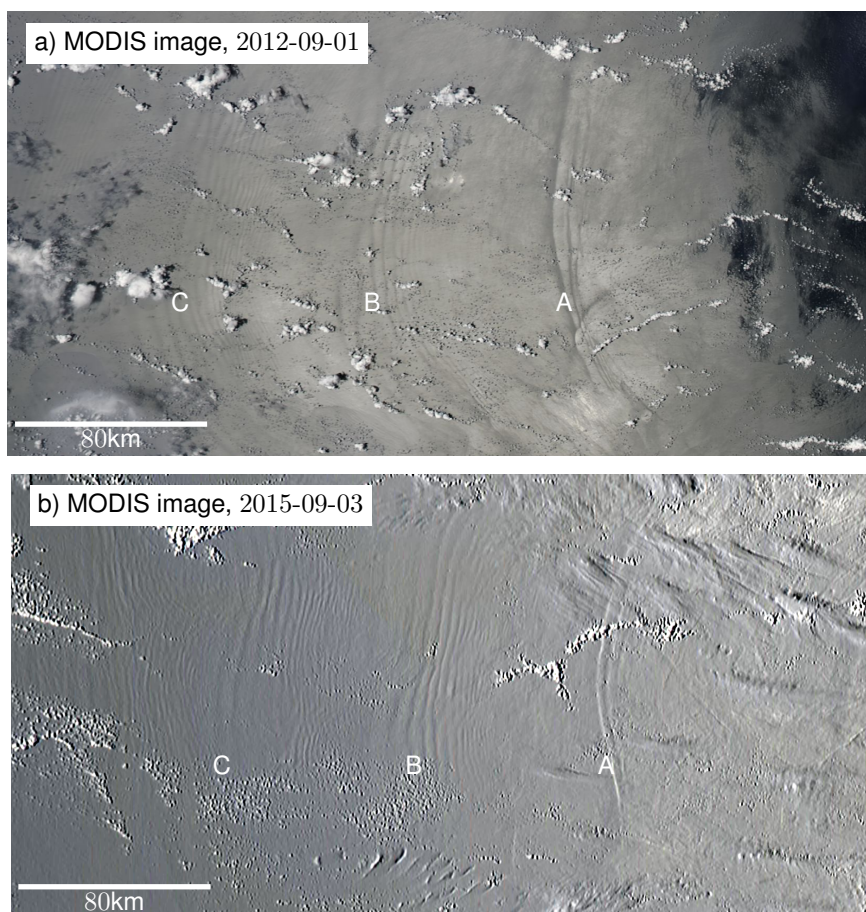
Figure 11. Internal wave packets in MODIS imagery from Aves Escarpment. MODIS sunglint imagery from dates in (a) 2012 and (b) 2015 (digitally enhanced) exhibits the surface expression of three packets of internal waves, at longitudes marked A, B, and C. Remarkably, similar wave packets are visible in imagery from 2018-09-05 (not shown). The largest packet, A, is located at Aves Ridge ($14°20'$N, $296°30'$E) on Aves Escarpment.

6 Discussion

The results of this study provide a descriptive snapshot of AMSEAS forecast skill during one 2-year period, and they are presumably dependent upon the particular ocean observing system, numerical model resolution and configuration, and data assimilation algorithm used during this period. Nonetheless, the results provide some insight into the capabilities and limitations of such a system for predicting and explaining high-frequency ocean variability. For example, it is evident in Figure 10b that the wavelength peak associated with the mode-2 phase-locked tides (red line) occurs at a slightly longer wavelength than the nearby peaks in either the high-frequency forecast (black line) or the forecast error (green line). In fact, an examination of the model output (not shown) indicates that the high-frequency forecast and forecast error associated with the 60 km wavelength peak is related to the non-linear mode-1 baroclinic tide generated on the shoals of the Aves Escarpment, while the 70 km peak
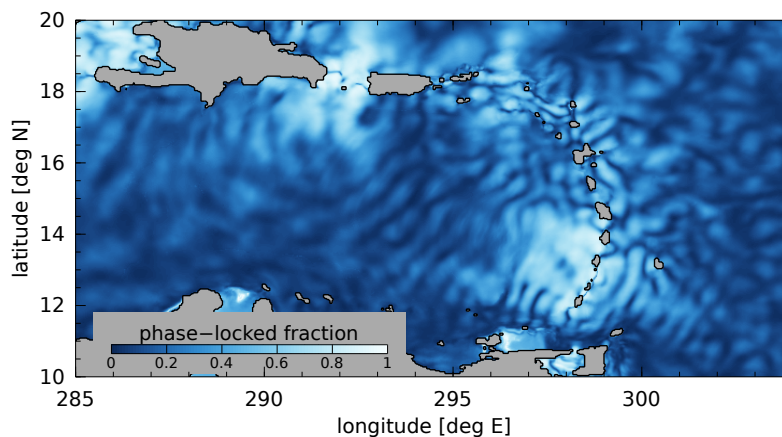
Figure 12. Fraction of variance, phase-locked versus total high-frequency variance (phase-locked plus non-phase-locked variance).

in the phase-locked tide is related to the mode-2 baroclinic tide. The nonlinear mode-1 dynamics are apparently AMSEAS'
rendition of the internal wave packets generated along Aves Escarpment which have been identified in satellite sun-glint
imagery (Alfonso-Sosa, 2013) and are the cause of coastal sieches around Puerto Rico (Giese et al., 1990; Alfonso-Sosa,
2015), nearly 1000 km to the northwest. Figure 10b indicates that a considerable fraction of the variance associated with these

5 waves is predictable by the AMSEAS system, even though is it not phase-locked with the astronomical tidal forcing (Giese
et al., 1990). Indeed, a brief search of the MODIS sunglint imagery found the pair of images displayed in Figure 11 in which
similar wavepackets are found in images taken 3 years apart.

A dedicated study of the dynamics responsible for both the predictable and unpredictable high-frequency variability would
be needed to understand the factors responsible for the time-variable propagation of the baroclinic tide, and its generation. The

10 high-frequency forecast error is correlated with the low-frequency forecast error (Fig. 9), but the reason for this correlation
has not been examined in detail. It was initially hypothesized that errors in location or intensity of (low-frequency) forecast
mesoscale eddies would be the cause of errors in the high-frequency forecasts; however, there are other possible explanations
for this relationship. For example, the generation of higher baroclinic modes and nonlinear overtides near Aves Ridge depends
the near-surface stratification at this site, and there are many factors which might influence this, aside from the location of

15 mesoscale eddies. Another explanation for the correlated errors is related to how the observed SLA data are assimilated with
the NCODA system, which projects the observations onto sub-surface profiles of temperature and salinity. The presence of
non-phase-locked tidal signals in the observations might be erroneously attributed to mesoscale features and assimilated into
the model; in this case, the low-frequency error would be caused by the high-frequency variability, rather than vice versa.

Present efforts to map the baroclinic tide with satellite altimeter data are generally only capable of identifying the phase-

20 locked part of the tidal signals (Ray and Mitchum, 1996; Carrère et al., 2004). Attempts to quantify the energy transport,
and dissipation, of the baroclinic tide from altimetry data must make assumptions about the partitioning of energy between

the phase-locked and non-phase-locked tides; however, present estimates for non-phase-locked tidal steric height suffer from sampling limitations (Zilberman et al., 2011; Kelly et al., 2015; Zaron, 2015, 2017). Ocean models are increasingly being used to study this quantity (Shriver et al., 2014; Kerry et al., 2016; Savage et al., 2017; Ansong et al., 2017), and AMSEAS is presently one of the highest-resolution models which includes both tides and wind-driven circulation. The ratio of phase-locked to total high-frequency steric height variance shown in Figure 12 indicates that the phase-locked tide dominates the variance – hence energy – only within a few hundred kilometers of the generation sites in the Caribbean Sea. The baroclinic tide in the middle of the Caribbean Sea is dominated by the non-phase-locked component. Whether or not this result is more broadly applicable is unknown, but the variance fraction is a useful diagnostic of the partition between open-ocean versus boundary dissipation of the baroclinic tide (Zaron, 2019).

Finally, an important caveat with the present study is related to the use of self-verifying analyses to assess the forecast errors. This approach is capable of measuring the predictability of the high-frequency steric height only to the extent that AMSEAS accurately represents the ocean dynamics. This approach is not capable of identifying systematic errors shared by the analysis and the forecast, and it thus provides a lower bound on the actual forecast error. To estimate this quantity, consider the root-mean-square goodness-of-fit to the assimilated SLA, which is roughly $\sigma = 6$ cm (Zaron et al., 2015). Assuming this value is the sum of independent components of instrumental measurement error, $\sigma_e = 3$ cm; baroclinic tide signal, $\sigma_t = 4$ cm (treated as "representation error" in the NCODA assimilation); and unknown analysis error, σ_a; one may use $\sigma_e^2 + \sigma_t^2 + \sigma_a^2 = \sigma^2$ to estimate $\sigma_a = 3$ cm. This is a lower bound for the analysis error at the measurement sites, as it does not account for the larger error between the satellite ground tracks. If $\sigma_a = 3$ cm is taken as the lower bound on the low-frequency forecast error, then Figure 9 suggests that 0.75 cm is a lower bound on the high-frequency forecast error. This is crude estimate which does not account for the geographic variability of either the ocean dynamics or the ocean observing system, but it provides a guide to the best case which may be attained in practice.

7 Conclusions

This study has examined the predictability of non-phase-locked baroclinic tides using four-day ocean forecast products from the AMSEAS system. It was motivated by the desire to understand our present capability for predicting baroclinic tidal SLA, which is expected to be a key limitation for measuring mesoscale and submesoscale processes with the forthcoming SWOT wide-swath satellite altimeter (Callies and Wu, 2019). The AMSEAS system is well-suited to this task since it represents the state-of-the-art among data-assimilating ocean forecast systems; it has resolution sufficient to realistically represent baroclinic tide generation and propagation, and the four-day forecast cycle is adequate to separate the SLA signals of low-frequency balanced motions from high-frequency processes, the latter being dominated by baroclinic tides.

The findings of this study indicate that a substantial fraction of non-phase-locked tidal sea level variability may be predictable with an ocean forecasting system. This result has been demonstrated using self-verifying analyses with the AMSEAS system, and future studies should investigate how to use independent high-frequency data to verify forecast skill statistics. The small

Ocean Science

Discussions

Open Access

EGU

scale and spatial inohomogeneity of the baroclinic tide makes this a challenging task. Nonetheless, many applications of altimetry which regard tidal SLA as a source of noise would benefit from improved predictions of baroclinic tidal sea level.

Code and data availability. The software and data products used in this research are available from the author.

Appendix A: Comparisons of observed and predicted phase-locked tides in the Caribbean

5 Tables A1 and A2 provide quantitative comparisons of the phase-locked tide sea surface height at tide gauges (and one bottom pressure sensor, DART-42407) in the Caribbean Sea for the main semi-diurnal and diurnal tides, M_2 and K_1. The observed data come from three sources, the National Data Buoy Center (for the DART buoy), the NOAA Center for Operational Oceanographic Products, and historical stations in Kjerfve (1981), as indicated in Table A1.

The amplitude and Greenwich phase of the AMSEAS sea surface height and observed height are listed. The station number 10 in the first column corresponds to the location in Figure 3. Stations located too close to distinguish on the map are indicated with lower-case letters in the Tables, e.g., "7a Barbuda" and "7b Antigua".

Over-all, the observed and predicted tides agree within a centimeter or two at most stations, with a few interesting exceptions. Because tides are relatively small in the Caribbean, the M_2 fractional errors are large, particularly in the northeast (e.g., stations 3, 5, and 6), near the M_2 amphidromic point (Kjerfve, 1981). Because the tide gauge measurements cannot distinguish 15 barotropic and baroclinic sea level, it may be that much of the error can be attributed to small scale differences in the baroclinic tide. The amplitude errors for K_1 are small, less than a centimeter almost everywhere, but a widespread phase error is present, except, oddly, at stations 8a and 8b on Guadaloupe. The reason for the K_1 phase error is obscure, but it may be related to the fact that K_1 behaves like a standing wave, so its phase may be strongly influenced by wave reflection at both open boundaries and the coastline in the AMSEAS model.

Ocean Science
Discussions

Table A1. Tide gauge stations and tidal statistics: M_2

	station	location [°W, °N]	H [cm]/ G [°] obs.	H [cm]/ G [°] mod.	H [cm]/ G [°] Δ, mod.-obs.
1	DART-42407[a]	(68.22,15.29)	2.5/134	3.1/145	0.6/10
2	Mona Island, Puerto Rico[b]	(67.94,18.09)	1.5/011	0.3/053	-1.2/42
3a	Magueyes Island, Puerto Rico[b]	(67.05,17.97)	0.8/023	1.5/106	0.7/83
3b	Penuelas, Puerto Rico[b]	(66.76,17.97)	0.8/039	0.1/316	-0.7/-83
4	San Juan, Puerto Rico[b]	(66.12,18.46)	15.9/020	15.5/016	-0.4/-4
5a	St. Thomas Harbor, USVI[c]	(64.93,18.33)	3.6/027	8.0/012	4.4/-15
5b	Cruz Bay, USVI[c]	(64.80,18.34)	0.4/284	7.8/012	7.4/88
5c	Lameshur Bay, USVI[b]	(64.72,18.32)	4.7/024	3.6/021	-1.1/-3
6a	Lime Tree Bay, USVI[b]	(64.75,17.69)	1.3/328	1.2/089	-0.1/121
6b	Christiansted Harbor, USVI[b]	(64.70,17.75)	3.5/346	2.9/355	-0.6/9
7a	Barbuda[b]	(61.82,17.59)	3.8/287	3.3/308	-0.5/21
7b	Antigua[c]	(61.79,17.16)	4.8/256	3.2/266	-1.6/10
8a	Sainte Rose, Guadaloupe[c]	(61.70,16.33)	6.5/241	5.0/229	-1.5/-12
8b	Pointe-a-Pitre, Guadaloupe[c]	(61.53,16.23)	8.7/233	5.8/227	-2.9/-6
9	Dominica[c]	(61.40,15.29)	11.7/216	7.5/214	-4.2/-2
10	Forte de France, Martinique[c]	(61.05,14.58)	5.5/211	9.7/212	4.2/1
11	Castries, St. Lucia[c]	(61.00,14.02)	9.4/191	10.7/209	1.3/18
12	Barbados[c]	(59.63,13.10)	22.9/227	19.5/216	-3.4/-11
13	Tobago Cays, Grenadines[c]	(61.35,12.63)	12.2/210	13.2/208	1.0/-2
14	Tobago[c]	(60.73,11.18)	29.3/218	23.6/212	-5.7/-6
15	Nariva River, Trinidad[c]	(61.03,10.40)	34.7/220	27.4/223	-7.3/3
16	Gaspar Grande, Trinidad[c]	(61.65,10.67)	29.3/225	15.9/250	-13.4/25
17	Carupano, Venezuela[c]	(63.25,10.67)	11.3/190	7.5/209	-3.8/19
18a	Amuay, Venezuela[c]	(70.22,11.75)	10.3/252	3.9/238	-6.4/-14
18b	Zaparita, Venezuela[c]	(71.65,11.02)	42.2/270	14.5/288	-27.7/18
19	Oranjestad, Aruba[c]	(70.05,12.52)	4.0/161	4.5/158	0.5/-3
20	Rio Hacha, Columbia[c]	(72.92,11.55)	6.6/127	7.5/140	0.9/13

[a] National Data Buoy Center, station 42407, http://www.ndbc.noaa.gov.

[b] NOAA Center for Operational Oceanographic Products and Services, http://tidesandcurrents.noaa.gov.

[c] Kjerfve (1981).

Ocean Science
Discussions

Open Access

EGU

Table A2. Tide gauge stations and tidal statistics: K_1

		location	H [cm]/ G [°]		
	station	[°W, °N]	obs.	mod.	Δ, mod.-obs.
1	DART-42407	(68.22,15.29)	8.8/236	9.0/221	0.1/-15
2	Mona Island, Puerto Rico	(67.94,18.09)	9.3/237	8.8/218	-0.5/-19
3a	Magueyes Island, Puerto Rico	(67.05,17.97)	8.0/233	8.3/218	0.3/-15
3b	Penuelas, Puerto Rico	(66.76,17.97)	8.2/234	8.2/221	-0.0/-13
4	San Juan, Puerto Rico	(66.12,18.46)	9.0/228	8.9/215	-0.1/-13
5a	St. Thomas Harbor, USVI	(64.93,18.33)	8.0/233	8.1/210	0.1/-23
5b	Cruz Bay, USVI	(64.80,18.34)	7.2/220	8.2/211	1.0/-9
5c	Lameshur Bay, USVI	(64.72,18.32)	8.3/229	8.4/215	0.1/-14
6a	Lime Tree Bay, USVI	(64.75,17.69)	8.3/237	8.4/220	0.1/-17
6b	Christiansted Harbor, USVI	(64.70,17.75)	8.2/229	8.4/215	0.2/-13
7a	Barbuda	(61.82,17.59)	7.2/229	7.7/216	0.5/-13
7b	Antigua	(61.79,17.16)	7.6/234	7.9/217	0.3/-17
8a	Sainte Rose, Guadaloupe	(61.70,16.33)	7.7/218	8.2/219	0.5/1
8b	Pointe-a-Pitre, Guadaloupe	(61.53,16.23)	7.3/220	8.2/219	0.9/-1
9	Dominica	(61.40,15.29)	10.2/231	8.5/221	-1.7/-10
10	Forte de France, Martinique	(61.05,14.58)	7.8/246	8.7/221	0.9/-25
11	Castries, St. Lucia	(61.00,14.02)	8.6/238	8.9/222	0.3/-16
12	Barbados	(59.63,13.10)	9.3/239	8.9/222	-0.4/-17
13	Tobago Cays, Grenadines	(61.35,12.63)	10.4/243	9.2/224	-1.2/-19
14	Tobago	(60.73,11.18)	9.6/244	9.6/225	-0.0/-19
15	Nariva River, Trinidad	(61.03,10.40)	7.6/247	10.3/229	2.7/-18
16	Gaspar Grande, Trinidad	(61.65,10.67)	6.7/244	11.2/233	4.5/-11
17	Carupano, Venezuela	(63.25,10.67)	10.4/238	11.0/231	0.6/-7
18a	Amuay, Venezuela	(70.22,11.75)	12.4/243	11.6/232	-0.8/-11
18b	Zaparita, Venezuela	(71.65,11.02)	13.6/250	13.7/241	0.1/-9
19	Oranjestad, Aruba	(70.05,12.52)	9.0/241	9.6/224	0.6/-17
20	Rio Hacha, Columbia	(72.92,11.55)	9.1/240	9.3/226	0.2/-14

Ocean Science
Discussions

References

Alfonso-Sosa, E.: First MODIS Images Catalog of Aves Ridge Solitons in the Caribbean Sea (2008-2013), working notes published on the author's web site, https://www.academia.edu/5500852/First_MODIS_Images_Catalog_of_Aves_Ridge_Solitons_in_the_Caribbean_Sea_2008-2013, 33 pages, 2013.

5 Alfonso-Sosa, E.: Seiches Costeros de Puerto Rico, Ocean Physics Education, Puerto Rico, 2015.

Ansong, J. K., Arbic, B. K., Alford, M. H., Buijsman, M. C., Shriver, J. F., Zhao, Z., Richman, J. G., Simmons, H. L., Timko, P. G., Wallcraft, A. J., and Zamudio, L.: Semidiurnal internal tide energy fluxes and their variability in a global ocean model and moored observations, J. Geophys. Res., 122, 1882–1900, 2017.

Barron, C. N., Kara, A. B., Rhodes, R. C., Rowley, C., and Smedstad, L. F.: Validation Test Report of the $1/8°$ Global Navy Coastal Ocean

10 Model Nowcast/Forecast System, Tech. Rep. NRL/MR/7320–07-9019, Naval Research Laboratory, Stennis Space Center, MS, 2007.

Callies, J. and Wu, W.: Some expectations for submesoscale sea surface height variance spectra, J. Phys. Oceanogr., p. in review, 2019.

Carrère, L., Le Provost, C., and Lyard, F.: On the statistical stability of the M_2 barotropic and baroclinic tidal characteristics from along-track TOPEX/Poseidon satellite altimetry analysis, J. Geophys. Res., 109, C03 033, 2004.

Carton, J. A. and Chao, Y.: Caribbean Sea eddies inferred from TOPEX/POSEIDON altimetry and a $1/6°$ Atlantic Ocean model simulation,

15 J. Geophys. Res., 104, 7743–7752, 1999.

Centurioni, L. R. and Niiler, P. P.: On the surface currents of the Caribbean Sea, Geophys. Res. Lett., 30, 1279, 2003.

Colosi, J. A. and Munk, W.: Tales of the venerable Honolulu tide gauge, J. Phys. Oceanogr., 36, 967–996, 2006.

Cummings, J. A.: Ocean Data Quality Control, in: Operational Oceanography in the 21st Century, edited by Schiller, A. and Brassington, G. B., pp. 91–121, Spinger, New York, 2011.

20 Dushaw, B. D.: Mapping low-mode internal tides near Hawaii using TOPEX/POSEIDON altimeter data, Geophys. Res. Lett., 29, 10.1029/2001GL013 944, 2002.

Egbert, G. D. and Erofeeva, S. Y.: Efficient Inverse Modeling of Barotropic Ocean Tides, J. Atm. and Ocean. Tech., 19, 183–204, 2002.

Gaultier, L., Ubelmann, C., and Fu, L.-L.: The Challenge of Using Future SWOT Data for Oceanic Field Reconstruction, J. Atm. and Ocean. Tech., 33, 119–126, 2016.

25 Giese, G. S., Chapman, D. C., Black, P. G., and Fornshell, J.: Causation of Large-Amplitude Coastal Seiches on the Caribbean Coast of Puerto Rico, J. Phys. Oceanogr., 20, 1449–1458, 1990.

Hernandez, F., Blockley, E., Brassington, G. B., Davidson, F., Divakaran, P., Drevillon, M., Ishizaki, S., Garcia-Sotillo, M., Hogan, P. J., Lagemaa, P., Levier, B., Martin, M., Mehra, A., Mooers, C., Ferry, N., Ryan, A., Regnier, C., Sellar, A., Smith, G. C., Sofianos, S., Spindler, T., Volpe, G., Wilkin, J., Zaron, E. D., and Zhang, A.: Recent progress in performance evaluations and near real-time assessment

30 of operational ocean products, J. Oper. Oceanogr., 8, 221–238, 2015.

Hogan, T. F., Liu, M., Ridout, J. A., Peng, M. S., Whitcomb, T. R., Ruston, B. C., Reynolds, C. A., Eckermann, S. D., Moskaitis, J. R., Baker, N. L., McCormack, J. P., Viner, K. C., McLay, J. G., Flatau, M. K., Xu, L., Chen, C., and Chang, S. W.: The Navy Global Environmental Model, Oceanography, 27, 116–125, 2014.

IOC, SCOR, and IAPSO: The international thermodynamic equation of seawater–2010: Calculation and use of thermodynamic properties,

35 Tech. Rep. 56, Intergovernmental Oceanographic Commission, Manuals and Guides, 2010.

Kara, A. B., Barron, C. N., Martin, P. J., Smedsted, L. F., and Rhodes, R. C.: Validation of interannual simulations from the $1/8°$ global Navy Coastal Ocean Model (NCOM), Ocean Mod., pp. 376–398, 2006.

Kelly, S. M., Jones, N. L., Ivey, G. N., and Lowe, R. J.: Internal tide spectroscopy and prediction in the Timor Sea, J. Phys. Oceanogr., 45, 64–83, 2015.

Kerry, C. G., Powell, B. S., and Carter, G. S.: Quantifying the incoherent M_2 internal tide in the Philippine Sea, J. Phys. Oceanogr., 46, 2457–2481, 2016.

5 Kjerfve, B.: Tides of the Caribbean Sea, J. Geophys. Res., 86, 4243–4247, 1981.

Metzger, E. J., Smedstad, O. M., Thoppil, P. G., Hurlburt, H. E., Cummings, J. A., Wallcraft, A. J., Zamudio, L., Franklin, D. S., Posey, P., Phelps, M. W., Hogan, P. J., Bub, F. L., and DeHaan, C. J.: US Navy operational global ocean and Arctic ice prediction systems, Oceanography, 27, 32–43, 2014.

Munk, W. H. and Cartwright, D. E.: Tidal spectroscopy and prediction, Phil. Trans. Roy. Soc. A, 259, 533–581, 1966.

10 Nero, R. W., Cook, M., and Coleman, A. T.: Using an ocean model to predict likely drift tracks of sea turtle carcasses in the north central Gulf of Mexico, Endangered Species Research, 21, 191–203, 2013.

O'Conner, B. S., Muller-Karger, F. E., and Redwood, R. W.: The role of Mississippi River discharge in offshore phytoplankton blooming in the northeastern Gulf of Mexico during August 2010, Remote Sensing of the Environment, 173, 133–144, 2016.

Privé, N. C. and Errico, R. M.: Spectral analysis of forecast error investigated with an observation system similation experiment, Tellus, 67,
15 25 977, 2015.

Rainville, L. and Pinkel, R.: Propagation of low-mode internal waves through the ocean, J. Phys. Oceanogr., 36, 1220–1236, 2006.

Ray, R. D. and Mitchum, G. T.: Surface manifestation of internal tides generated near Hawaii, Geophys. Res. Lett., 23, 2101–2104, 1996.

Ray, R. D. and Zaron, E. D.: Non-stationary internal tides observed with satellite altimetry, Geophys. Res. Lett., 38, L17 609, https://doi.org/10.1029/2011GL048617, 2011.

20 Ray, R. D. and Zaron, E. D.: M_2 internal tides and their observed wavenumber spectra from satellite altimetry, J. Phys. Oceanogr., 46, 3–22, 2016.

Rosmond, T. E., Teixeira, J., Peng, M., Hogan, T. F., and Pauley, R.: Navy Operational Global Atmospheric Prediction System (NOGAPS): Forcing for ocean models, Oceanography, 15, 99–108, 2002.

Savage, A. C., Arbic, B. K., Alford, M. H., Ansong, J. K., Farrar, J. T., Menemenlis, D., O'Rourke, A. K., Richman, J. G., Shriver, J. F., Voet,
25 G., Wallcraft, A. J., and Zamudio, L.: Spectral decomposition of internal gravity wave sea surface height in global models, J. Geophys. Res., 122, 7803–7821, 2017.

Shriver, J. F., Richman, J. G., and Arbic, B. K.: How stationary are the internal tides in a high-resolution global ocean circulation model?, J. Geophys. Res., 119, 2769–2787, 2014.

Solano, M., Canals, M., and Leonardi, S.: Development and validation of a coastal ocean forecasting system for Puerto Rico and the U.S.
30 Virgin Islands, J. of Ocean Eng. and Sci., 3, 223–236, 2018.

Torres, R. R. and Tsimplis, M. N.: Tides and long-term modulations in the Caribbean Sea, J. Geophys. Res., 116, C10 022, 2011.

Torres, R. R. and Tsimplis, M. N.: Seasonal sea level cycle in the Caribbean Sea, J. Geophys. Res., 117, 2012.

Zaron, E. D.: Non-stationary internal tides inferred from dual-satellite altimetry, J. Phys. Oceanogr., 45, 2239–2246, 2015.

Zaron, E. D.: Mapping the Non-Stationary Internal Tide with Satellite Altimetry, J. Geophys. Res., 122, 539–554, 2017.

35 Zaron, E. D.: Baroclinic Tidal Sea Level from Exact-Repeat Mission Altimetry, J. Phys. Oceanogr., 49, 193–210, 2019.

Zaron, E. D. and Egbert, G. D.: Verification Studies for a z-coordinate primitive-equation model: tidal conversion at a mid-ocean ridge, Ocean Mod., 14, 257–278, 2006.

Zaron, E. D. and Rocha, C. B.: Meeting Summary: Internal Gravity Waves and Meso/Submesoscale Currents in the Ocean: Anticipating High-Resolution Observations from the SWOT Swath Altimeter Mission, Bull. Am. Met. Soc., 99, 2018.

Zaron, E. D., Chavanne, C., Egbert, G. D., and Flament, P.: Baroclinic tidal generation in the Kauai Channel inferred from HF-Radar, Dyn. Atm. and Oceans, 48, 93–120, 2009.

5   Zaron, E. D., Fitzpatrick, P. J., Cross, S. L., Harding, J., Bud, F. L., Wiggert, J. D., Ko, D. S., Lau, Y., Woodard, K., and Mooers, C. N.: Initial evaluations of a Gulf of Mexico/Caribbean ocean forecast system in the context of the Deepwater Horizon disaster, Front. of Earth Sci., 9, 605–636, 2015.

Zhao, Z., Alford, M. H., Girton, J., Johnston, T. M., and Carter, G.: Internal tides around the Hawaiian Ridge estimated from multisatellite altimetry, J. Geophys. Res., 116, 2011.

10   Zhao, Z., Alford, M. H., Girton, J. B., Rainville, L., and Simmons, H. L.: Global Observations of Open-Ocean Mode-1 M_2 Internal Tides, J. Phys. Oceanogr., 46, 1657–1684, 2016.

Zilberman, N. V., Merrifield, M. A., Carter, G. S., Luther, D. S., Levine, M. D., and Boyd, T. J.: Incoherent nature of M_2 internal tides at the Hawaiian Ridge, J. Phys. Oceanogr., pp. 3021–3036, 2011.